Validation of a Transient 3-D CFD Mars Rotorcraft Performance Simulation Using Experimental Data

Validation of a Transient 3-D CFD Mars Rotorcraft Performance Simulation Using Experimental Data

Manuel Carreño Ruiz * and Domenic D'Ambrosio †
Department of Mechanical and Aerospace Engineering, Politecnico di Torino, Torino, 10124, Italy

Isaac S. Bensignor‡ and Matthew McCrink§
The Ohio State University Aerospace Research Center, Columbus, Ohio, 43235 USA

Given the success of NASA/JPL's *Ingenuity* helicopter, the study of Martian flight vehicles and their aerodynamic characteristics has become a rapidly growing field of research. At NASA Ames, the "Rotor Optimization for the Advancement of Mars eXploration" (ROAMX) team and their partners have published designs for an advanced, second generation Mars helicopter – the "Mars Science Helicopter" (MSH) – which possesses a novel rotor geometry. This paper presents the independent development and validation of a numerical model for assessing Mars rotorcraft performance, which uses an MSH-inspired rotor as the primary research artifact. Performing Mars-analogous or exact recreations of Mars environmental conditions on Earth is both a costly and difficult technical challenge. Therefore, a transient, 3-D unsteady Reynolds-Averaged Navier Stokes (RANS) CFD model is proposed to estimate the performance of an MSH-inspired rotor in Earth atmospheric conditions. The experimental data presented in this paper corresponds to a sweep of collectives for a 75% span rotor Reynolds numbers of $2.87 * 10^5$. The numerical simulations use the results of the experimental campaign to validate the accuracy and fidelity of the model. Delayed Detached Eddy Simulations (DDES) and a computationally cheaper steady-state RANS approach were validated using experimental data at low thrust conditions. Then, the RANS approach was used to sweep different collective pitch angles for both nominal and modified twist geometries that attempt to account for aeroelastic deformations using low-fidelity modeling. The blades with a modified twist show an improved agreement with the experimental data, with errors of ~5% in the thrust and torque coefficients for low collectives. For large collective angles, beyond which the figure of merit peaks, the RANS simulations predict premature stall compared to the experimental data. The methods and results presented in this paper are the first phase of an effort to independently estimate both the aerodynamics and dynamics of such a unique rotor geometry.

I. Nomenclature

A	=	Rotor disk area, $\pi R^2, m^2$
C_Q	=	Torque coefficient, $Q/\rho(\Omega R)^2 RA$
C_Q/σ	=	Torque loading coefficient
C_T	=	Thrust coefficient, $T/\rho(\Omega R)^2 A$
C_T/σ	=	Blade loading coefficient
c	=	Airfoil, rotor chord, m
FM	=	Figure of merit, $C_T^{3/2}/\sqrt{2}\, C_Q$
k	=	Turbulent kinetic energy, $m^2 s^{-2}$
M	=	Mach number, $V/\sqrt{\gamma RT}$
N_b	=	Number of rotor blades per rotor disk
Q	=	Rotor torque, $N\ m$

*PhD Candidate, Department of Mechanical and Aerospace Engineering, Politecnico di Torino, manuel.carreno@polito.it
†Adjunct Professor, Department of Mechanical and Aerospace Engineering, Politecnico di Torino, domenic.dambrosio@polito.it
‡Research Engineer, Department of Mechanical and Aerospace Engineering, AIAA Member, isaac.bensignor@gmail.com.
§Research Assistant Professor, Department of Mechanical and Aerospace Engineering, AIAA Senior Member. mccrink.2@osu.edu

Re	=	Reynolds number, $\rho V c/\mu$
R	=	Rotor radius, m, Gas constant, $m^2 s^{-2} k^{-1}$
T	=	Thrust, N, Temperature, K
V	=	Velocity, $m\ s^{-1}$
y^+	=	Dimensionless wall distance
γ	=	Ratio of specific heats
ρ	=	Fluid density, $kg\ m^{-3}$
σ	=	Rotor solidity, $N_b c R/\pi R^2$
Ω	=	Rotor rotational frequency, s^{-1}
ω	=	Specific dissipation rate, s^{-1}

II. Introduction

The study of Martian aerodynamics is a rapidly growing field of research. NASA/JPL's Martian helicopter, *Ingenuity*, continues to set records, aid the *Perseverance* rover in scouting ground paths, and expand its flight envelope. An uncommon aerodynamic regime exists for the rotor blades of a Martian rotorcraft vehicle: the cold, thin atmosphere results in high sub-sonic Mach numbers and low Reynolds numbers. Due to this extreme combination, there are numerous challenges related to understanding the aerodynamic and aeroelastic characteristics of a Martian flight vehicle. The low atmospheric pressure – less than 1% of Earth's at standard sea level conditions – significantly limits the thrust a rotor generates. Consequently, relatively large rotor solidities, rotation rates, and diameters are required [1]. The low gravitational acceleration on Mars – approximately 38% of that found on Earth – aids in reducing the significance of weight considerations, but only partially compensates for the negative effects associated with the atmosphere. To maximize the payload capacity and vehicle endurance of Martian rotorcraft, rotor efficiency must be enhanced, and classical optimal rotor considerations valid for rotorcraft flight on Earth may not apply.

Several studies have conducted numerical and experimental investigations of ultra-low Reynolds numbers, which is defined by the $Re = O(10^3 - 10^4)$ flow domain [2]. Kroo and Kunz [2] performed numerical studies on airfoils, while Kunz and Strawn[3] carried out numerical and experimental studies on rotors in ultra-low Reynolds number flows at low sub-sonic Mach numbers. The numerical studies performed by Refs. [2] and [3] relied upon a two-dimensional, incompressible Navier-Stokes flow solver. The main findings of those works indicate that ultra-low Reynolds numbers primarily lead to laminar flow and the generation of thickened boundary layers, effectively modifying the assessed geometry. At flight Reynolds numbers greater than 10^5, separation caused by sharp leading edges typically indicates the rapid onset of stall. However, this is uncommon in the ultra-low Reynolds number flow domain [2], which presents an unsteady high lift regime after leading edge separation.

Tohoku University in Sendai, Japan, houses a dedicated "Mars Wind Tunnel" designed for experimentally assessing compressible, low Reynolds number aerodynamics. This facility has provided extensive and insightful airfoil performance data for different geometries, as presented in Refs. [4–7]. These experimental efforts have been used to validate different numerical methods, ranging from high-order DNS solvers [8] to commercial finite volume Navier-Stokes solvers [9, 10]. Considering the significant impact the separation regions have on airfoil and rotor performance [11], it is crucial to simulate the unsteady and three-dimensional flow attributes for determining their impact on rotor performance. Although accurate numerical simulations of rotors are prohibitively expensive for optimization purposes, having a reliable and validated numerical tool capable of identifying unique flow features characterizing this regime is very interesting, given the challenges of experimentally replicating the Martian atmosphere.

NASA Ames, NASA/JPL, the University of Maryland, AeroVironment Inc., and Tohoku University have partnered to design, build, and test aspects of NASA's second-generation Martian flight vehicle known as the "Mars Science Helicopter" (MSH) [12]. Previous and on-going design work from, but not limited to NASA and their university and industry collaborators [1, 11–24], University of Maryland [25–28], JAXA [5, 29–31], Politecnico di Torino [10, 32–34] and ONERA [35, 36] have aided in substantiating vehicle design ideas and configurations, airfoil selection and analyses, optimal rotor design and scaling, vehicle sizing considerations, and identification of exploration sites of interest for a Martian rotorcraft. A brief summary of the activities involved in the MSH design is described herein for completeness.

At NASA Ames, the "Rotor Optimization for the Advancement of Mars eXploration" (ROAMX) team and their colleagues have invested significant efforts in computational modeling, numerical analysis, and experimental research efforts to study the complex flow phenomena occurring during Martian rotorcraft flight, including but not limited to Refs. [12, 13, 16–18, 26, 37, 38]. Accurately simulating compressible, low Reynolds number flow for Martian rotorcraft performance estimation has become increasingly important to support Mars exploration efforts [12], especially

considering the expense of conducting experiments under similar conditions. As a result of ROAMX's optimization efforts, a novel rotor geometry has been proposed for use on the MSH [1, 12], and its performance and geometry are the primary area of focus for this work.

The following sections describe the numerical and experimental campaigns of this research endeavour. The numerical model is presented in terms of mesh-grid generation, the employed fundamental governing equations, the discretization scheme, and additional turbulence and wake modeling packages. The numerical method implemented is based on the compressible Reynolds Averaged Navier-Stokes (RANS) equations, chosen for the non-negligible importance of modeling turbulence for the Reynolds numbers at which the blade will operate. The effects of enhanced wake turbulence modeling are analyzed through Delayed Detached Eddy Simulations (DDES). By using different methods from those applied by the ROAMX team, the list of applicable numerical tools and methods validated for estimating the performance of "Mars-optimized" rotors and the compressible, low Reynolds numbers domain grows wider and becomes increasingly accessible to the broader research community.

The experiment is described with respect to the critical hardware used, along with a brief description of the manufacturing method employed for the rotor blades. A blade based on an 85.3% scaled MSH rotor was manufactured using composite materials and tested at several collectives and one rotation rate under Earth atmospheric conditions. The validation described herein, using terrestrial data, was performed at Reynolds numbers exceeding 250,000, which is over an order of magnitude higher than those found in Martian conditions. Despite the differences in boundary layer state, the validation is important for checking the agreement with the experimental tests, understanding the complexities of grid generation for a polygonal-like rotor, and identifying inconsistencies between experimental and numerical results. These inconsistencies, for example, can be caused by not accounting for aeroelastic or experimental recirculation effects. Subsequently, a description of the numerical and experimental test matrices is provided. The results of the verification study are addressed, along with a comparison of different numerical approaches and a discussion of the first-order modeling employed for estimating aeroelastic effects that deformed the blade. The paper concludes with a discussion of the study's most notable results and a brief presentation of a future research framework.

III. Materials and Methods

A. Rotor Blade Geometry

Below, in Fig. 1, is an adapted representation of the novel MSH rotor geometry from Johnson et al. [1] highlighted with the airfoil sections that define specific spanwise locations. A simple linear loft connects the defined spanwise locations with rectilinear plate-like sections. Johnson et al. [1] presents the preliminary blade design and describes that the rotor's leading and trailing edges come to a sharp point throughout the entire span. Moreover, between the 7% span location and the rotor tip, there is -18° of twist. The airfoils shown at the 50%, 75%, and 100% span correspond most closely to the "Double Edged Plate" (DEP) airfoil geometry optimized by Koning et al. [19, 20] for compressible, low Reynolds number flow (i.e. $Re = 1.67 * 10^4$, $M = 0.52$). The airfoils shown for the inboard spanwise locations are of increased thickness to accommodate sufficiently rigid integration of the rotor with the hub [1]. However, the sharp and polygonal-like features of the DEP are retained in these most inboard sections for preserving the spanwise continuity of the rotor geometry. The DEP airfoil forces the flow to separate at the leading edge and reattaches forming a separation bubble. The periodic coherent shedding of vortical structures over the top of the airfoil aids in lift generation at low Reynolds numbers, similar to the flapping flight mechanics of insects and birds [11, 19]. An equivalent interpretation of this phenomenon is presented by Carreño Ruiz et al. [33], which associates the improvement of the efficiency of these airfoils to the presence of an optimal separation bubble that enhances the lift with a small drag penalization due to the reduced skin friction.

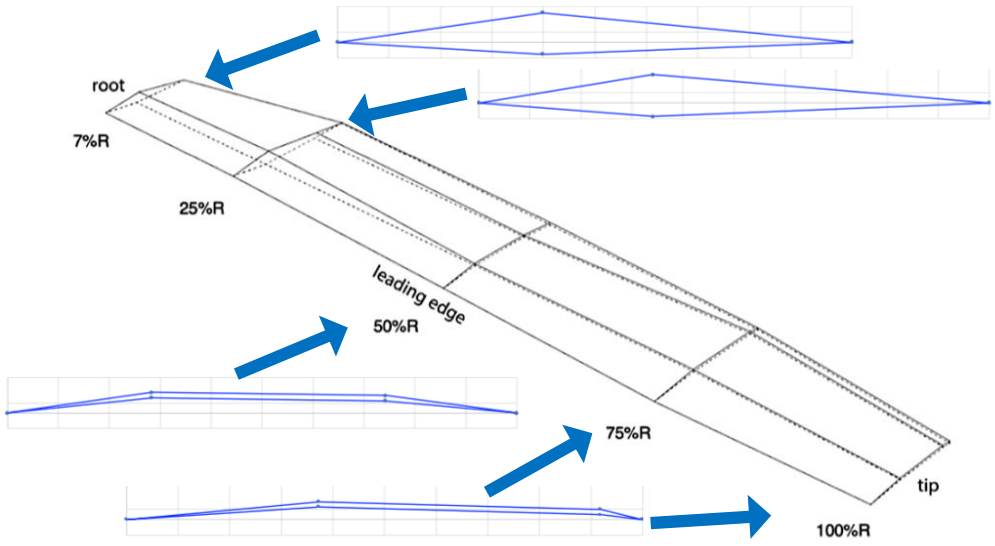

Fig. 1 Isometric view of the MSH hexacopter blade design. Adapted from Johnson et al. [1]

B. Numerical Simulations

This work presents two approaches to simulate rotor flows; an unsteady Delayed Detached Eddy Simulation (DDES) approach and a steady RANS approach using STAR-CCM+. The compressible RANS equations were used as the mathematical model in the simulations. The evaluation of the viscous fluxes uses a second-order approximation. In contrast, the calculation of inviscid fluxes uses a third-order Monotonic Upwind Scheme for Conservation Laws (MUSCL) blended with a third-order central differences reconstruction method combined with Roe's scheme. Furthermore, the unsteady model employs a second-order implicit time integration method, whereas the steady approach utilizes an implicit pseudo-time marching scheme to drive the pre-conditioned system of equations to convergence.

1. Computational Domain and Grid

The computational domain is modeled as a truncated cone with all the walls placed over 10 rotor radii from the rotor to prevent wall/ground/ceiling interference during the simulated physical time, as shown in Fig. 2. The computational grid used in the unsteady simulations consists of approximately 40 million polyhedral cells with prism layers near the blade to adequately capture the strong wall-normal gradients in the boundary layer. The y^+ is maintained below 1 for the whole blade surface. The thin geometry of the blade requires a large cell count near the leading and trailing edges. This can be appreciated by the blade surface mesh shown in Figs. 3 – 5. The wake is refined for an extension of one rotor diameter using a cell size 12 times smaller than the chord at the tip, then it progressively coarsens to avoid an excessive cell count. This validation is based on integral loads, and therefore resolving a long wake would drastically increase the computational cost without causing a relevant impact on the rotor performance predictions. However, it is important to resolve the wake vortex system near the blades well to accurately model Blade Vortex Interaction (BVI).

In the case of steady RANS simulations, we make use of a periodic boundary condition and simulate just a third of the domain used in the transient simulation. To avoid convergence issues that typically occur in steady-state solutions of hovering rotors with a small thrust coefficient, we substituted wall boundaries for far-field conditions with a residual axial velocity component. We also distinguish in this case two regions, a static region used to adequately impose boundary conditions and a rotating region in which we solve the RANS equations in a rotating reference frame. Despite some differences in the grid caused by the presence of the periodic boundary conditions and the slightly larger rotating domain to allow for the development of the wake, the near-body and wake resolution are maintained obtaining an overall cell count of ~14 million.

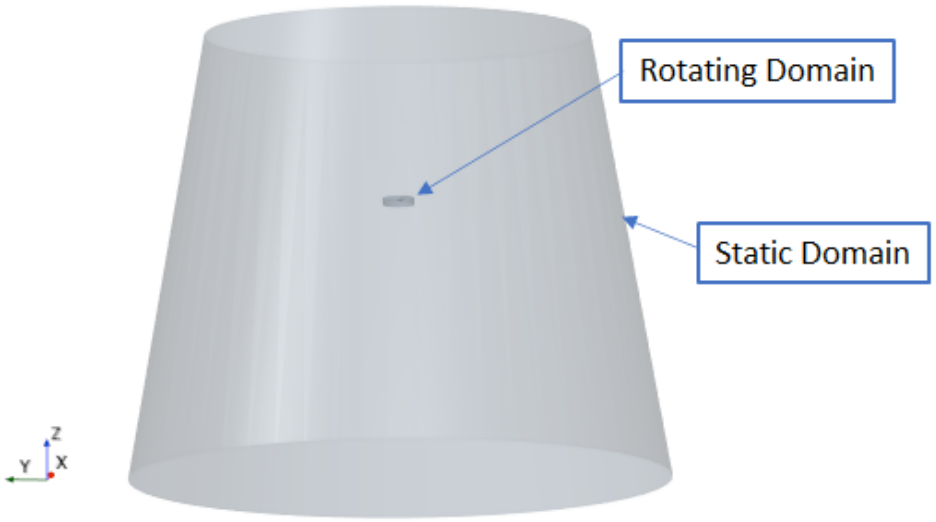

Fig. 2 Computational domain.

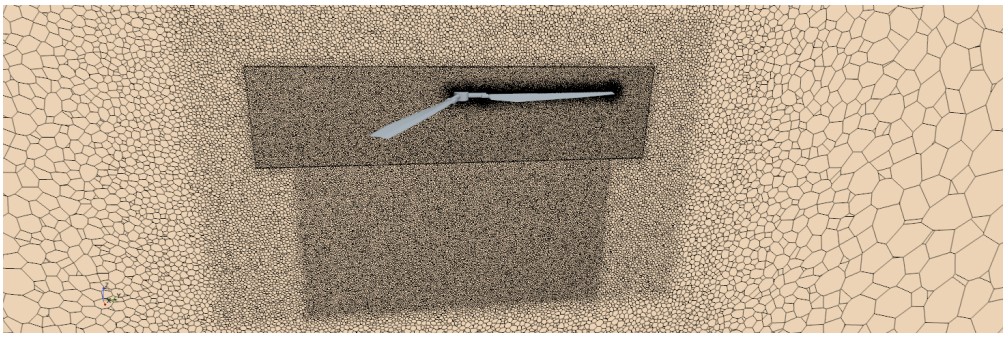

Fig. 3 Computational grid at plane X = 0 m.

Fig. 4 Surface grid over the rotor.

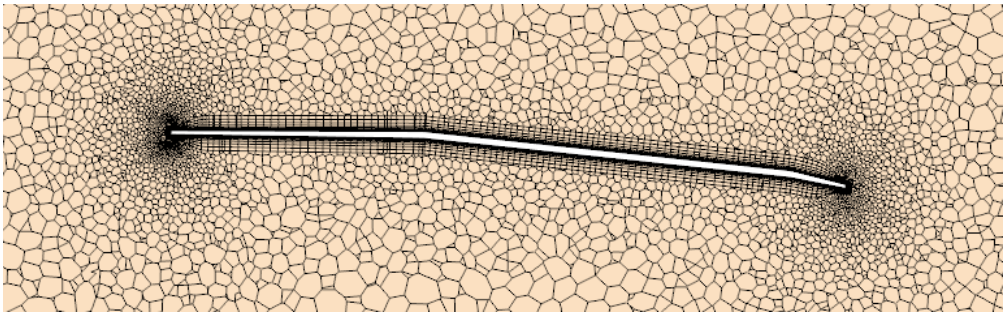

Fig. 5 Prism layer details at plane Y = 0.5 m.

2. Turbulence modeling

The results of the simulations rely on computations using the two equation $k-\omega$ shear stress transport eddy viscosity model presented by Menter [39]. This model has been successfully employed to estimate aerodynamic loads on rotors, including in works by Bergmann et al. [40] and Carreño Ruiz et al. [41]. The rectangular leading edge geometry creates separation bubbles on the pressure and suction sides when the blade is fixed at a zero degree tip angle of attack. These bubbles are small but increase in size for larger pitch angles. For the zero pitch condition, we also present a DDES using the approach proposed by Menter et al. [42]. This method blends the aforementioned $k-\omega$ shear stress transport model in regions where the grid resolution is insufficient to capture the inertial scales (e.g. boundary layers) with LES capabilities in regions where larger eddies can be resolved. A similar approach using the DDES methodology proposed by Spalart [43] has been demonstrated successfully by Yoon et al. [44] and Ventura Díaz et al. [45] for different scale rotors using *OVERFLOW*. In this work we use the finite volume solver STAR-CCM+. In particular, the DDES simulations have been performed using a third-order central difference scheme with a 5% upwinding for stability purposes.

3. Rotation Modeling

The rotation of the grid in the DDES simulation is modeled with a sliding grid approach. A rotating inner region slides within a static outer region. Both regions are interfaced using an AMI (Arbitrary Mesh Interface) protocol. Initially, we carried out ten revolutions at a time step of 2.5 degrees per temporal iteration and five revolutions at a time step of 1 degree per temporal iteration. The first revolutions with a larger time step allow the flow to develop by advecting the starting vortex downstream. Then, successive iterations with a smaller time step ensure a time-accurate solution. The steady RANS approach uses a Moving Reference Frame (MRF) to model the rotation of the blade while maintaining a static grid. The RANS equations are formulated in a rotating reference frame which results in extra source terms in the momentum equations associated with centrifugal and Coriolis accelerations.

C. Mars Rotor Test Stand and 85% Scaled Blade Design

The Mars Rotor Test Stand used in the experiments is shown in Fig. 6a and is first described by Bensignor et al. [46]. For completeness and to reflect updates to the hardware, the experimental setup is described in brief. Select components of the test stand are labeled, including the FUTEK MBA500 889.6 N, 25.6 N m load cell, the torque and thrust transfer shaft, the passive vibration isolating interface, and the fully articulated rotor head swashplate mechanism. Moreover, the rotor stand is considered "out of ground effect" with respect to the testing room, as there are no obstructions within two rotor radii in the wake propagation direction [47]. Experimental performance of the rotor was captured in terms of thrust generated and torque produced and are presented non-dimensionally as blade loading coefficient, C_T/σ, torque loading coefficient, C_Q/σ and figure of merit, FM.

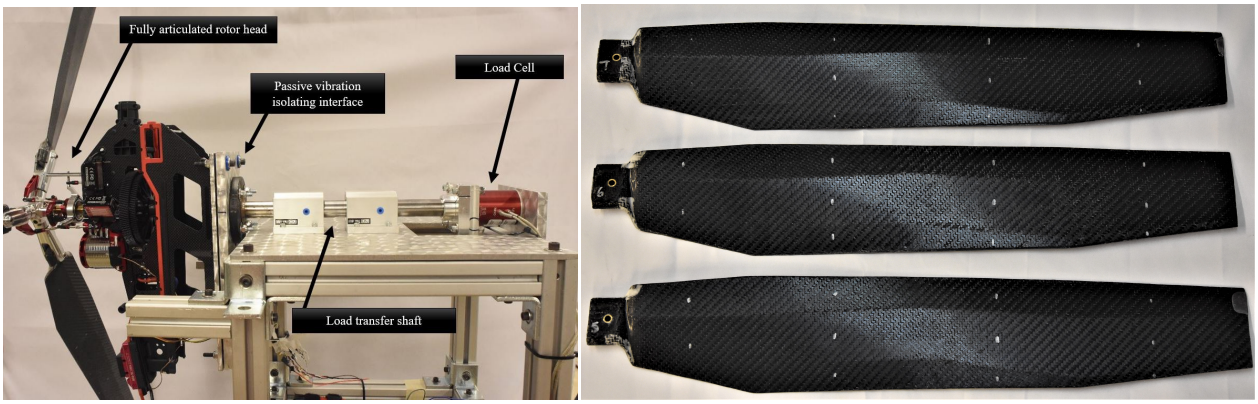

(a) Profile test stand view. **(b) Manufactured rotor blades**

Fig. 6 Select components and rotors used on the Mars Rotor Test Stand

To avoid confusion, the rotors manufactured that are based on and inspired by the MSH design will be referred to as the "scaled rotors." The scaled rotors are shown in Fig. 6b. They are sized at 85.3% full scale of the MSH and have a total span length of 0.546 m. The rotor head paddle/blade root attachment point is 0.096 m radially offset from the rotor rotational axis. The root of the scaled rotors extends 0.016 m inboard from the connection point to provide sufficient structural support along the centrifugal loading axis. The tip radius is 0.6259 m, and the disk area is 1.23 m^2. The MSH rotor solidity is 0.142 [1], however, due to the scaling and the rotor blade attachment point offset, the solidity of the scaled rotors manufactured is 0.108. The 85.3% scaling was chosen such that two rotor diameters could fit between the rotor rotational axis and the vacuum chamber facility wall to be used in future experiments.

To produce a structurally rigid internal core, fiberglass reinforced epoxy resin, a brass tube for rotor head integration, a 100% infill 3-D printed root insert, and strands of carbon fiber tow comprised the internal make-up of the rotor blade. Although all rotor blades were built using the same layup technique, it is possible that the stiffness and mass attributes of each blade differ due to small variations in material properties associated with the composite layup method and human factors. Early destructive testing of the scaled rotors determined that the method used was sufficiently strong and resulted in a solidly filled rotor blade.

Extensive quantification of the rotor thickness, twist, weight, and center of mass location were performed on the set of blades used in the experiment to ensure consistency and sufficient characterization. These measurements were performed using digital calipers and a rotor balancing tool and were repeated several times. The average of the measured linear fits characterizing the twist rate demonstrated a 0.845% error with respect to CAD model of the rotor. Due to the downsized scaling of the rotor, and material constraints, the scaled rotor set was nominally thicker along the span compared to the CAD model. However, each plate section thickness measured demonstrated no more than a 1.2 mm difference then the CAD design criteria. The rotor set has an average mass of 164.02 g and a standard deviation of 0.081 g (i.e. the blades were balanced to less than a 1/10th of a gram difference). In summary, the scaled rotor blades are quantitatively and qualitatively similar to the CAD model of the blade. The reader may refer to a set of manufactured blades by ROAMX in Ref. [12] for a visual and qualitative comparison of the blades described herein.

D. Test Conditions

The numerical simulations spot check results from the experimental data obtained at an average RPM of 998. The resultant 75% span Reynolds number and tip Mach number are $2.87 * 10^5$ and 0.190, respectively. The 75% span location is at a radial distance 0.469 m and has a chord length of 0.091 m. (Note that the 75% span location is not where the 75% airfoil is located as depicted by Fig. 1 due to the rotor head paddle/blade root attachment offset.) The density and temperature used in the simulations correspond to $\rho = 1.177\ kg/m^3$ and $T = 300\ K$, which are within 3 % of the experimental conditions for all collective angles. The electronic speed controller used in the experiments attempts to maintain the given RPM input, however, small fluctuations do occur. Thus, an average RPM is presented for each sweep of collectives. This averaged RPM is used to define the rotation rate in the numerical simulations.

IV. Rotor Performance Results

This section presents both numerical and experimental results. First, preliminary flow visualizations generated with the numerical model demonstrate some of the interesting aerodynamic phenomena occurring for the zero pitch condition. Next, select experimental results are presented and are then compared with the results of the numerical simulation for different pitch conditions. The collective angle is defined relative to the rotor tip angle of attack for the experiments performed. For the deformed rotor blade conditions assessed below, the collective was referenced in the simulation via the root-hub.

A. Numerical Results and Flow Visualization at Zero Degrees Collective Pitch

Simulations have been computed for the zero-pitch condition using both a DDES and a steady RANS approach, as shown in the previous section. The former approach is computationally exhaustive while the latter allows a reduction of CPU cost of around an order of magnitude. This reduction is achieved partially by simulating only one-third of the domain profiting from the axial symmetry of the rotor and boundary conditions. An additional reduction is obtained by using a steady-state approach to drive the solution to convergence.

Table 1 compares the blade loading coefficients and figure of merit obtained experimentally with the numerical results using the aforementioned approaches. RANS and DDES simulations exhibit discrepancies within approximately 5%. Both sets of results are in good agreement with the experimental values. To further explore the differences between these numerical approaches, Fig. 7 presents the blade loading and torque loading coefficient distributions along the radial coordinate. The influence of BVI is notably intense, featuring a characteristic inflection point in the thrust per unit length distribution, which is well captured by both approaches. Figure 8 shows how the tip vortex impinges the blade in the outboard sections causing the aforementioned blade loading distribution. On the other hand, the torque per unit length is in good agreement towards the inboard stations but towards the tip, RANS calculations slightly underestimate the value predicted with the DDES. Considering the intense BVI in this region, the steady nature of the approach, and the differences in turbulence modeling, discrepancies in the torque coefficient of approximately 5% may be anticipated. The important reduction in CPU time and the good agreement demonstrated suggest that steady RANS modeling is an interesting alternative for rotor performance predictions in this Reynolds number regime. The simulations presented in this work were computed using 96 cores from three Intel Xeon Scalable Processors Gold 6130 operating at 2.10 GHz. The computations were performed at the high-performance computing facility of Politecnico di Torino (HPC@POLITO).

Figure 9 shows how the leading edge geometry produces separation bubbles on the suction and pressure sides of the blade. These are characterized by a reversed flow creating a negative chordwise wall shear stress. Figure 10 shows how these bubbles are relatively small but extend for almost the entire radial coordinate on the suction side and the outboard sections on the pressure side. The pressure side bubble will disappear for higher pitch angles, but the suction side bubble will grow with increasing collective angle. The suction side separation bubble occurs by design as it reduces skin friction for Reynolds numbers below 20,000, at which this blade is designed to operate. These bubbles are found to be steady in the rotating reference frame in both DDES and RANS approaches at the zero pitch condition.

Table 1 Comparison between numerical and experimental results for the scaled rotor blade at zero collective pitch.

	Thrust Coefficient ($\times 10^{-3}$)	Torque Coefficient ($\times 10^{-4}$)	Figure of Merit	CPU hours
RANS	6.84	6.90	0.580	1,980
DDES	6.95	7.30	0.561	14,400
Experimental	6.74	7.08	0.553	-

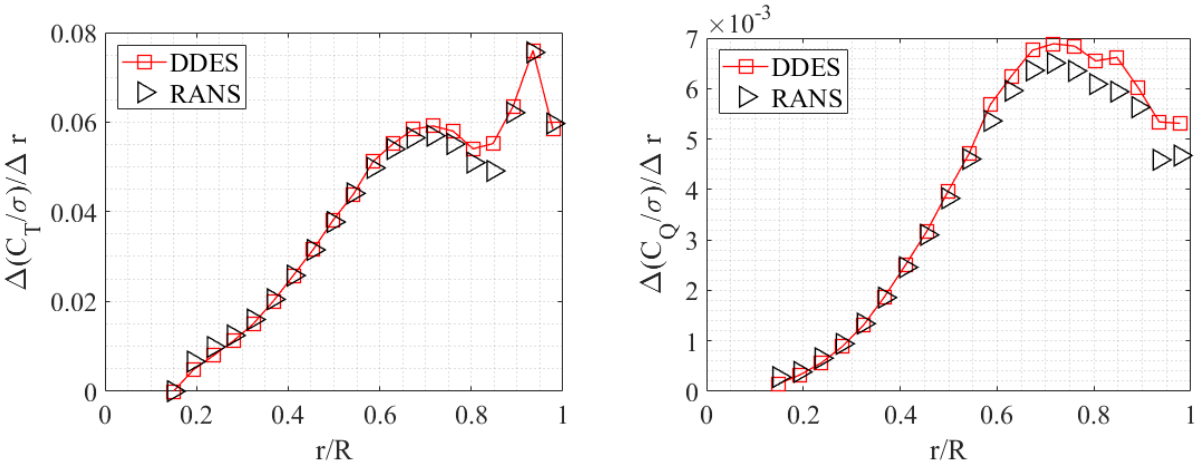

(a) Thrust coefficient distribution.

(b) Torque coefficient distribution.

Fig. 7 Radial distribution of loads for DDES and RANS approaches.

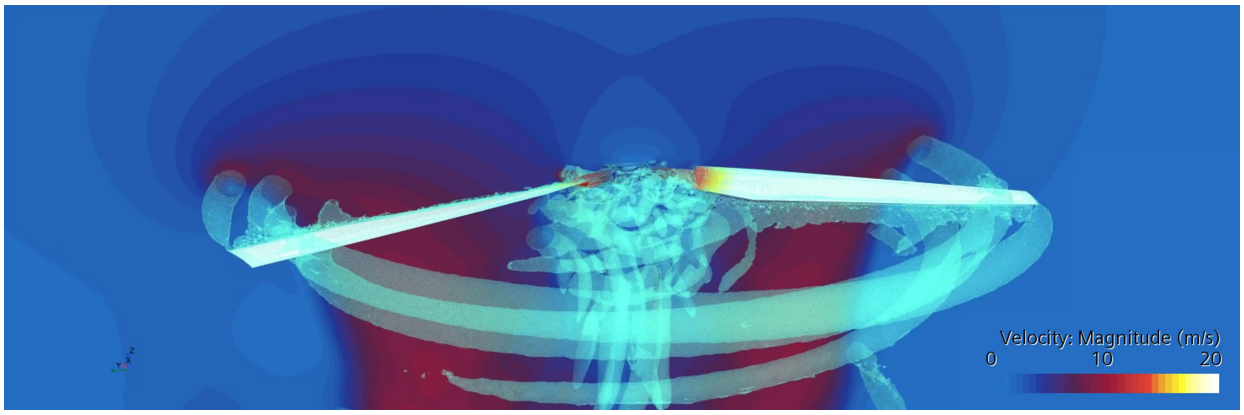

Fig. 8 Velocity magnitude in plane section X = 0 m. Q-criterion isosurface at $Q = 2000/s^2$. Delayed Detached Eddy Simulation.

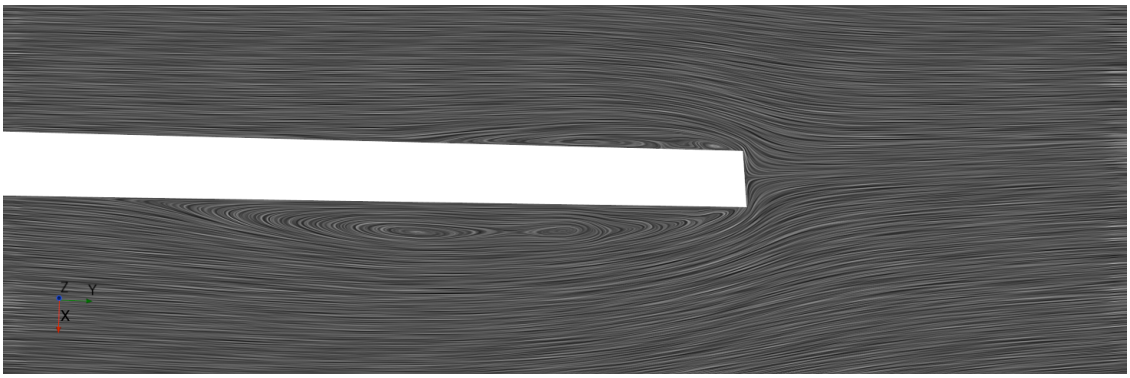

Fig. 9 Line convolution integral of the blade relative velocity field at the leading edge. Radial section placed at 0.5 m from the hub. RANS simulation.

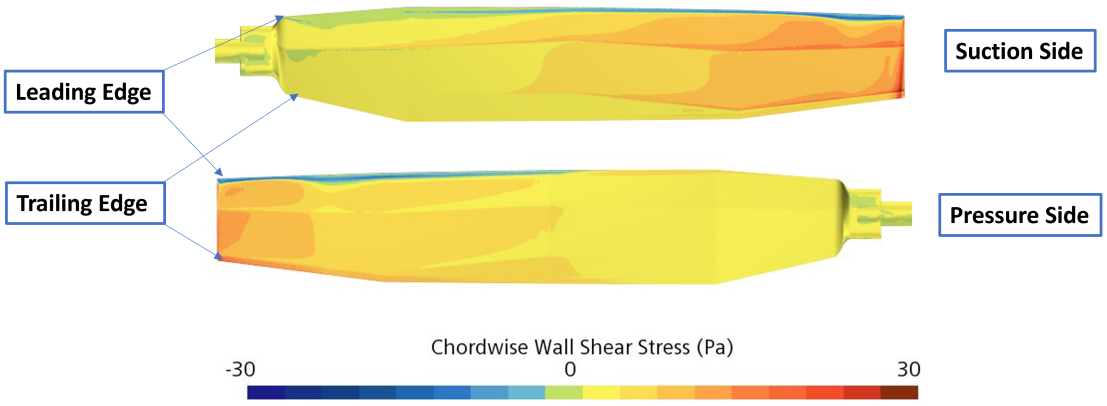

Fig. 10 Chordwise wall shear stress on the rotor blades. RANS simulation.

B. Modifying the Rotor Twist Rate Due to Aeroelastic Effects

With increasing load due to increasing rotational speed and/or collective, the MSH rotor would deform and result in a nose-up pitching behavior in the outboard 50% span due to a combination of the trapeze effect and propeller moment, as described by Chi et al. [26]. The trapeze effect is relevant to consider for thin structural members that are twisted and are subject to a tensile load. The "untwisting phenomena" dictated by the trapeze effect is dependent on the twist rate alone. However, due to inertial and aerodynamic forces, the trapeze effect's affect on the twist is modified by the propeller moment in a manner that is a direct function of the collective angle assessed. The deformation is known to be most significant in the outboard section of the rotor (i.e. >56% span for the scaled rotor; >50% span for the MSH rotor), where the rotor reaches a 1% thickness to chord ratio. At higher thickness to chord ratios, the trapeze effect is seemingly insignificant in modifying a blade's twist rate [26]. This deformation response is described in detail by Chi et al. [26], who studied nearly an identical rotor as presented in this paper (which was first described by Johnson et al. [1]). Similar analysis with respect to the aeroelastic considerations for thin, Mars optimized rotors is also discussed by Lumba et al. [18] and Wright et al. [38].

Figure 11 qualitatively demonstrates that aeroelastic effects were present in terms of blade bending and twisting. The deformations photographed were not used for a quantitative aeroelastic or aeromechanical analysis, but for justifying the use of a twist modification. The scale included in the figure is purely for reference and for making order of magnitude approximations in the tip deflection and twist. When a 1 cm rotation about the quarter chord of the tip airfoil in the loading direction is assumed – which is plausible based on the observations – trigonometric principles dictates that a 10 degree geometric rotation of the tip airfoil can occur. Six degrees of additional twist was chosen to assess its impact on rotor performance based on the aforementioned observations. The twist rate was modified beginning at the 50% airfoil location (i.e. the 56% span location). The overall twist rate modeled is no longer linear, but piece-wise linear and is a function of the collective angle assessed. Instead of adding the additional twist statically to all analyses, a scaled amount based on the tip collective assessed was added to the blade's geometry. For example, at zero degrees of collective, zero additional twist added; at nine degrees of collective, six degrees of twist added (i.e. a tip angle of 15 degrees). As discussed by Chi et al. [26] and Lumba et al. [18], the aeroelastic effects are a function of the blade collective. The twist rate modifications made are demonstrated in Fig. 12.

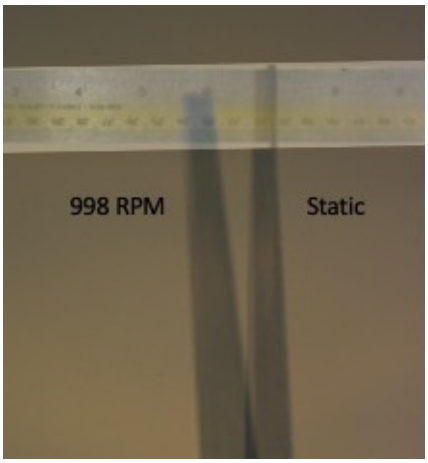

Fig. 11 Representative scaled rotors tip deflection. Photos overlaid from static, $\alpha_{tip} = 0°$ position and 998 RPM at $\alpha_{tip} = 8°$.

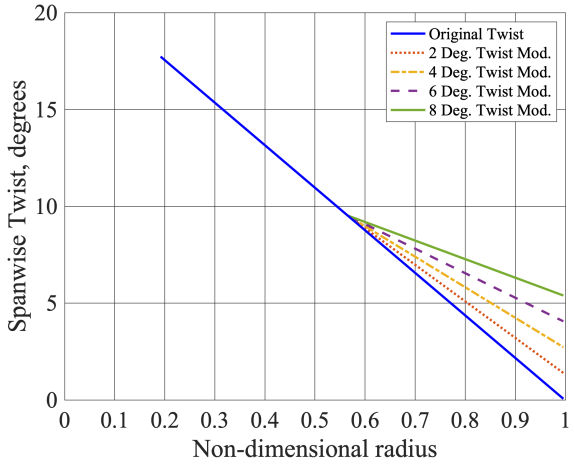

Fig. 12 Modifications to the blade twist rate for different collective angles assessed

C. Comparison of the RANS Numerical Simulation with Experimental Performance at Different Pitch Conditions

Figures 13 – 16 demonstrate the experimental and simulated performance of the scaled rotors. Figure 13 shows the blade loading coefficient vs. the collective angle. Figure 14 shows the torque loading coefficient vs. the collective angle. Figure 15 shows torque loading coefficient vs. blade loading coefficient. Lastly, Fig. 16 shows the figure of merit vs. the blade loading coefficient. As a result of the linear twist distribution starting with 18^o at the inboard stations and the camber of the airfoils, the figure of merit at 0° of collective is not zero, like an untwisted symmetric rotor blade would be. The results of the numerical simulations clearly show how the inclusion of the additional twist to model blade deformation helps to capture the experimental trends for blade loading and torque loading coefficients up to four degrees collective angle. When the collective is at six degrees, the RANS calculations for the deformed geometry predict a premature stall compared to experiments. The onset of stall can be identified by the increase in the slope of the torque loading coefficient vs. blade loading coefficient curve and the drop in the figure of merit. Premature stall is possibly associated with the use of a steady RANS model for presenting a relevant leading edge separation. In these cases, steady approaches typically find large separated regions while time-accurate approaches predict a leading edge vortex shedding that increases both lift and drag. Until the onset of this regime, steady RANS is capable of accurately predicting blade performance including the peak value of the figure of merit and the blade loading coefficient at which it is obtained.

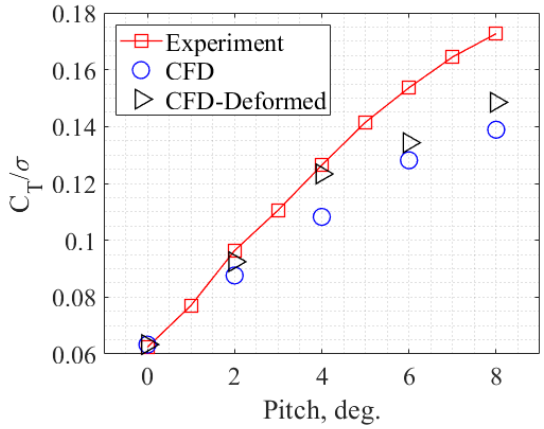

Fig. 13 Experimental and Numerical Blade Loading Coefficient vs. Collective Angle

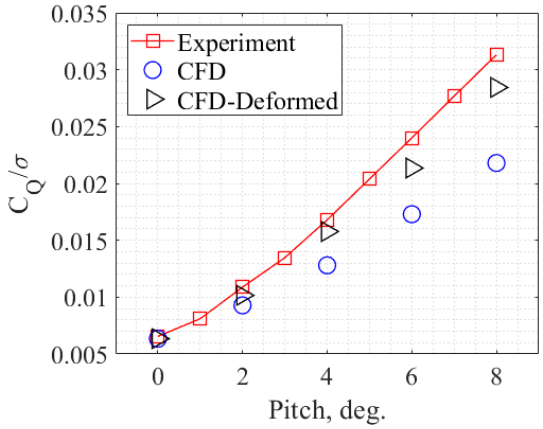

Fig. 14 Experimental and Numerical Torque Loading Coefficient vs. Collective Angle

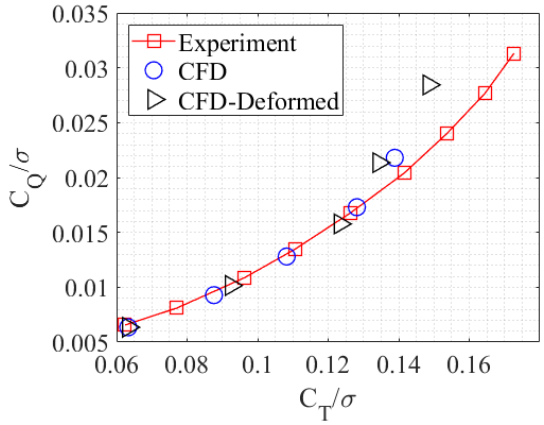

Fig. 15 Experimental and Numerical Torque Loading Coefficient vs. Thrust Loading Coefficient

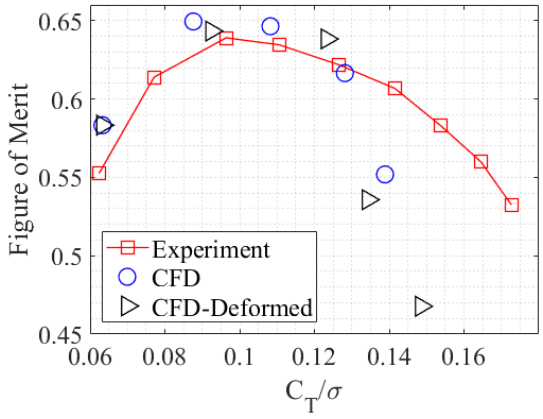

Fig. 16 Experimental and Numerical Figure of Merit vs. Blade Loading Coefficient

V. Conclusions and Future Work

This paper demonstrates the validation of a numerical model using experimental results to estimate the performance of a "Mars-optimized" rotor operating in Earth atmospheric conditions. The rotor is polygonal-like, presenting sharp leading edges and an apex that, at specific operating conditions, will cause separation. These geometric characteristics pose challenges in the definition of a well-resolved computational near-body grid. Using composite materials, an 85.3% scaled "Mars Science Helicopter"-inspired rotor blade was manufactured and tested at several collectives and a speed of 998 RPM. The measured peak efficiency was approximately 0.64 in terms of figure of merit, which occurred at a blade loading coefficient of 9.64×10^{-2} or a tip collective pitch of two degrees.

Steady RANS and DDES simulations have been compared at zero pitch conditions showing a satisfactory agreement with experimental data. RANS predictions of blade loading and torque loading coefficients presented noticeable underestimations at higher collective angles that were associated with the rigid modeling of the blades. Qualitative experimental observation of the blade deformation at the tip, deformations on similar blades reported in literature, and trigonometric considerations were used to modify the twist distribution of the blades to account for aeroelastic effects. Simulations were repeated for the deformed geometry showing substantial improvements in the prediction of experimental data. The RANS model accurately captured the peak figure of merit and the blade loading at which it is achieved, however, it predicts a premature stall for larger collective angles. Despite the flawed performance predictions at higher collectives, the good agreement until the peak figure of merit allows us to conclude that the aeroelastic effects are of paramount importance to adequately predict the performance of these extremely thin blades. Future work will address the deformation of these blades using a higher fidelity structural model loosely coupled with the CFD solver's predictions. Furthermore, high-fidelity CFD solutions will also be computed at higher collective angles in an attempt to capture rotor performance after the peak in the figure of merit where RANS models fail to capture the experimental trends.

Acknowledgments

The authors would like to acknowledge conversations with members of the NASA Ames ROAMX team for clarifying comments on some of the work discussed herein.

References

[1] Johnson, W., Withrow-Maser, S., Young, L., Malpica, C., Koning, W., Kuang, W., Fehler, M., Tuano, A., Chan, A., Datta, A., Chi, C., Lumba, R., Escobar, D., Balaram, J., Tzanetos, T., and Grip, H., "Mars Science Helicopter Conceptual Design," *NASA TM-2020-220485*, 2020.

[2] Kroo, I., and Kunz, P., "Analysis and Design of Airfoils for Use at Ultra-low Reynolds Numbers," *AIAA Aerodynamics for Micro Air Vehicle Applications*, 2001, pp. 35–60. https://doi.org/10.2514/5.9781600866654.0035.0060.

[3] Kunz, P., and Strawn, R., "Analysis and Design of Rotors at Ultra-low Reynolds Numbers," *40th AIAA Aerospace Sciences Meeting and Exhibit*, AIAA, Reno, Nevada, USA, 2002, p. 99.

[4] Munday, P. M., Taira, K., Suwa, T., Numata, D., and Asai, K., "Nonlinear lift on a triangular airfoil in low-Reynolds-number compressible flow," *Journal of Aircraft*, Vol. 52, No. 3, 2015, pp. 924–931.

[5] Anyoji, M., Nonomura, T., Aono, H., Oyama, A., Fujii, K., Nahai, H., and Asai, K., "Computational and Experimental Analysis of a High-Performance Airfoil Under Low-Reynolds-Number Flow Condition," *Journal of Aircraft*, Vol. 51, No. 6, 2014, pp. 1864–1872. https://doi.org/10.2514/1.C032553.

[6] Anyoji, M., Nose, K., Ida, S., Numata, D., Nagai, H., and Asai, K., "Low Reynolds Number Airfoil Testing in a Mars Wind Tunnel," *40th Fluid Dynamics Conference and Exhibit*, 2010. https://doi.org/10.2514/6.2010-4627.

[7] Suwa, T., Nose, K., Numata, D., Nagai, H., and Asai, K., "Compressibility Effects on Airfoil Aerodynamics at Low Reynolds Number," *30th AIAA Applied Aerodynamics Conference*, 2012. https://doi.org/10.2514/6.2012-3029.

[8] Caros, L., Buxton, O., Shigeta, T., Nagata, T., Nonomura, T., Asai, K., and Vincent, P., "Direct Numerical Simulation of Flow over a Triangular Airfoil Under Martian Conditions," *AIAA Journal*, Vol. 60, No. 7, 2022, pp. 3961–3972. https://doi.org/10.2514/1.J061454.

[9] Désert, T., Jardin, T., Bézard, H., and Moschetta, J.-M., "Numerical predictions of low Reynolds number compressible aerodynamics," *Aerospace Science and Technology*, Vol. 92, 2019, pp. 211–223. https://doi.org/10.1016/j.ast.2019.05.064.

[10] Carreño Ruiz, M., and D'Ambrosio, D., "Experimental Validation of Virtual Wind Tunnel Testing for Ultra-low Reynolds Numbers Flows," *Aerotecnica Missili & Spazio*, Vol. 103, No. 1, 2024.

[11] Koning, W., Romander, E., and Johnson, W., "Low Reynolds Number Airfoil Evaluation for the Mars Helicopter Rotor," *NASA ARC-E-DAA-TN53889*, 2018.

[12] Cummings, H., Perez, N. P., Koning, W., Johnson, W., Young, L., Haddad, F., Romander, E., Balaram, J., Tzanetoz, T., J.Bowman, and et al., "Overview and Introduction of the Rotor Optimization for the Advancement of Mars eXploration (ROAMX) Project," *Aeromechanics for Advanced Vertical Flight Technical Meeting*, Vertical Flight Society, San Jose, California, USA, 2022.

[13] Withrow-Maser, S., Koning, W., Kuang, W., and Johnson, W., "Recent Efforts Enabling Future Mars Rotorcraft Missions," San Jose, CA, USA, 2020.

[14] Young, L., Aiken, E., Derby, M., Demblewski, R., and Navarrete, J., "Experimental Investigation and Demonstration of Rotary-Wing Technologies for Flight in the Atmosphere of Mars," American Helicopter Society, Montreal, Canada,, 2002.

[15] Young, L., Delaune, J., Johnson, W., Withrow-Maser, S., Cummings, H., Sklyanskiy, E., Izraelevitz, J., Schutte, A., Fraeman, A., and Bhagwat, R., "Design Considerations for a Mars Highland Helicopter," 2020.

[16] Dull, C., Wagner, L., Young, L., and Johnson, W., "Hover and Forward Flight Performance Modeling of the Ingenuity Mars Helicopter," *Aeromechanics for Advanced Vertical Flight Technical Meeting*, Vertical Flight Society, 2022.

[17] Schatzman, N., Dominguez, M., Lee, P., and Young, L., "LILI (Long-term Ice-field Levitating Investigator) Mars Aerial and Ground Explorer for Martian Polar Regions," *Aeromechanics for Advanced Vertical Flight Technical Meeting*, Vertical Flight Society, 2022.

[18] Lumba, R., Chi, C., Datta, A., Koning, W., Perez-Perez, N., and Cummings, H., "Structural Design and Aeromechanical Analysis of Unconventional Blades for Future Mars Rotorcraft," *Aeromechanics for Advanced Vertical Flight Technical Meeting*, Vertical Flight Society, 2022.

[19] Koning, W., Romander, E., and Johnson, W., "Performance Optimization of Plate Airfoils for Martian Rotor Applications Using a Genetic Algorithm," *NASA ARC-E-DAA-TN71478*, 2019.

[20] Koning, W., Romander, E., and Johnson, W., "Optimization of Low Reynolds Number Airfoils for Martian Rotor Applications Using an Evolutionary Algorithm," *AIAA SciTech 2020 Forum*, AIAA, Orlando, Florida, USA, 2020, pp. 84–100. https://doi.org/10.2514/6.2020-0084.

[21] Koning, W., Johnson, W., and Allan, B., "Generation of Mars Helicopter Rotor Model for Comprehensive Analyses," *NASA ARC-E-DAA-TN50660*, 2018.

[22] Koning, W., "Airfoil Selection for Mars Rotor Applications," *NASA CR-2019-220236*, 2019.

[23] Koning, W., Johnson, W., and Grip, H., "Improved Mars Helicopter Aerodynamic Rotor Model for Comprehensive Analyses," *AIAA Journal 57, No. 9*, 2019, pp. 3969–3979. https://doi.org/10.2514/1.J058045.

[24] Argus, F., Ament, G., and Koning, W., "The Influence of Laminar-Turbulent Transition on Rotor Performance at Low Reynolds Numbers," *Technical Meeting on Aeromechanics for Advanced Vertical Flight*, Vertical Flight Society, San Jose, California, USA, 2020.

[25] Datta, A., Roget, B., Griffiths, D., and Pugliese, G., "Design of a Martian Autonomous Rotary-Wing Vehicle," *Journal of Aircraft Vol. 40, No. 3*, 2003, pp. 461–472. https://doi.org/10.2514/2.3141.

[26] Chi, C., Lumba, R., Jung, Y. S., and Datta, A., "Aeromechanical Analysis of a Next-Generation Mars Hexacopter Rotor," *Journal of Aircraft*, Vol. 59, No. 6, 2022, pp. 1463–1477. https://doi.org/10.2514/1.C036739.

[27] Chi, C., Datta, A., and Lumba, R., "Structural Design and Aeromechanical Analysis of a Next-Generation Mars Hexacopter Rotor," *Vertical Flight Society 77th Annual Forum & Technology Display*, 2021, pp. 1–23. https://doi.org/10.4050/F-0077-2021-16696.

[28] Escobar, D., Chopra, I., and Datta, A., "Vacuum Chamber Testing of 1.5 Foot Diameter Mars Rotor," American Helicopter Society, San Francisco, CA, USA, 2018.

[29] Tsuzuki, N., Sato, S., and Abe, T., "Conceptual Design and Feasibility for a Miniature Mars Exploration Rotorcraft," *Proceedings of the 24th International Congress of the Aeronautical Sciences*, International Congress of Aeronautical Sciences Paper 2004-1.8.2, Yokohama, Japan, 2004, pp. 1–10.

[30] Sugiura, M., Tanabe, Y., Sugawara, H., Kimura, K., Oyama, A., Sato, M., Yoshikawa, K., Buto, Y., Kanazaki, M., and et al., "Blade Shape Optimization of Mars Helicopter Exploring Pit Craters," Vertical Flight Society, Fort Worth, Texas, USA, 2022. https://doi.org/10.4050/F-0078-2022-17445.

[31] Uwatoko, K., Kanazaki, M., Nagai, H., Fujita, K., and Oyama, A., "Blade Element Theory Coupled with CFD Applied to Optimal Design of Rotor For Mars Exploration Helicopter," AIAA, 2020. https://doi.org/0.2514/6.2020-1284.

[32] Carreño Ruiz, M., and D'Ambrosio, D., "Aerodynamic optimization and analysis of quadrotor blades operating in the Martian atmosphere," *Aerospace Science and Technology*, Vol. 132, 2023, p. 108047. https://doi.org/10.1016/j.ast.2022.108047.

[33] Carreño Ruiz, M., Renzulli, L., and D'Ambrosio, D., "Airfoil optimization for rotors operating in the ultra-low Reynolds number regime," *Physics of Fluids*, Vol. 35, No. 10, 2023, p. 103603. https://doi.org/10.1063/5.0166170.

[34] Carreño Ruiz, M., "Numerical Simulation and Aerodynamic Design of Small-Scale Rotary-Wing for Unmanned Aerial Systems in Terrestrial and Martian Applications," Ph.D. thesis, Politecnico di Torino, 2023. Available: https://hdl.handle.net/11583/2982720.

[35] Bézard, H., Desert, T., Moschetta, J.-M., and Jardin, T., "Aerodynamic design of a Martian micro air vehicle," *EUCASS 2019*, MADRID, Spain, 2019. Available: https://hal.archives-ouvertes.fr/hal-02397054.

[36] Désert, T., Moschetta, J.-M., and Bézard, H., "Numerical and experimental investigation of an airfoil design for a Martian micro rotorcraft," *International Journal of Micro Air Vehicles*, Vol. 10, No. 3, 2018, pp. 262–272. https://doi.org/10.1177/1756829318794171.

[37] Withrow-Maser, S., Johnson, W., Young, L., Koning, W., Kuang, W., Malpica, C., Balaram, J., and Tzanetos, T., "Mars Science Helicopter: Conceptual Design of the Next Generation of Mars Rotorcraft," *Ascend 2020 Virtual Forum*, AIAA, 2018. https://doi.org/10.2514/6.2020-4029.

[38] Wright, S. J., Koning, W. J., Perez-Perez, B. N., Cummings, H. V., and Johnson, W., "Predicted Performance Effects of Blade Elasticity on Testing of Rotors for Mars," *Autonomous VTOL Technical Meeting*, Vertical Flight Society, Mesa, Arizona, USA, 2023.

[39] Menter, F. R., "Two-equation eddy-viscosity turbulence models for engineering applications," *AIAA Journal*, Vol. 32, No. 8, 1994, pp. 1598–1605. https://doi.org/10.2514/3.12149.

[40] Bergmann, O., Götten, F., Braun, C., and Janser, F., "Comparison and evaluation of blade element methods against RANS simulations and test data," *CEAS Aeronautical Journal*, Vol. 13, No. 2, 2022, pp. 535–557. https://doi.org/10.1007/s13272-022-00579-1.

[41] Carreño Ruiz, M., Scanavino, M., D'Ambrosio, D., Guglieri, G., and Vilardi, A., "Experimental and numerical analysis of hovering multicopter performance in low-Reynolds number conditions," *Aerospace Science and Technology*, Vol. 128, 2022, p. 107777. https://doi.org/10.1016/j.ast.2022.107777.

[42] Menter, F. R., and Kuntz, M., "Adaptation of eddy-viscosity turbulence models to unsteady separated flow behind vehicles," *The Aerodynamics of Heavy Vehicles: Trucks, Buses, and Trains*, Springer, 2004, pp. 339–352.

[43] Spalart, P. R., Deck, S., Shur, M. L., Squires, K. D., Strelets, M. K., and Travin, A., "A new version of detached-eddy simulation, resistant to ambiguous grid densities," *Theoretical and computational fluid dynamics*, Vol. 20, 2006, pp. 181–195. https://doi.org/10.1007/s00162-006-0015-0.

[44] Yoon, S., Chaderjian, N., Pulliam, T. H., and Holst, T., "Effect of Turbulence Modeling on Hovering Rotor Flows," *45th AIAA Fluid Dynamics Conference*, 2015. https://doi.org/10.2514/6.2015-2766.

[45] Ventura Diaz, P., and Yoon, S., "High-Fidelity Simulations of a Quadrotor Vehicle for Urban Air Mobility," *AIAA SciTech Forum 2022*, San Diego, CA, January 2022. https://doi.org/10.2514/6.2022-0152.

[46] Bensignor, I., Seth, D., and McCrink, M., "Rotor Propulsion Modeling for Low Reynolds Number Flow ($Re < 10^5$) for Martian Rotorcraft Flight," *AIAA Aviation Forum 2022*, 2022. https://doi.org/10.2514/6.2022-3958.

[47] Leishman, J. G., *Principles of Helicopter Aerodynamics*, Cambridge University Press, 2006. pp. 258-259.